JNP Journal of Nanophotonics

RESEARCH PAPER

Synthesis and characterization of thin films of P_3HT-G/MoS_2 nanocomposites in photodetectors applications

Nagham M. Obaid, Amer Al-Nafiey,* and Ghaleb Al-Dahash
University of Babylon, Collage of Sciences for Women, Hillah, Iraq

ABSTRACT. The nanocomposite, poly(3-hexylthiophene-2,5-diyl) (P_3HT)–graphene/molybdenum disulfide (MoS_2), was for the first time fabricated by the pulse laser ablation (PLA) method with different numbers of laser pulses deposited onto a porous silicon (PSi) substrate using the drop-casting technique. Nanocrystalline PSi films are prepared by electrochemical etching of a P-type silicon wafer. The optical properties, transmission electron microscope (TEM), and photodetector properties were studied. Optical measurements confirmed that the energy gap decreases from 2.03 to 1.87 eV with the increasing number of laser pulses for graphene and MoS_2. This decrease in the energy gap was attributed to the increase in graphene and its combination with molybdenum. Due to the higher electrical conductivity of the hybrid material, the MoS_2 leads to reduce the band gap. From the TEM images, it was found that the average size of the particles was between 3.1 and 20.8 nm depending on increasing the number of laser pulses for both graphene and MoS_2 with hemispherical particle shapes. The $Ag/PSi/P_3HT-G/MoS_2/Ag$ photodetector was fabricated for all samples prepared to characterize the effect of laser pulses number for graphene and MoS_2 on the photodetector performance. The maximum value of the specific response, specific detection, and quantum efficiency was 0.35 A/W, 5.1×10^{12} cm $Hz^{1/2}$ W^{-1}, and 49.2% at 900 nm due to the absorption edge of silicon around 0.23 A/W, 3.3×10^{12} cm $Hz^{1/2}$ W^{-1}, and 38.9% at 760 nm due to the absorption edge of P_3HT-G/MoS_2 NPS. The results indicate that the PLA method successfully fabricated the P_3HT-G/MoS_2 nanocomposites and that the resulting product exhibited high values in responsivity, detectivity, and quantum efficiency. Additionally, it appears that the nanocomposites may have enhanced the same parameters of the PSi photodetector.

 [DOI: 10.1117/1.JNP.17.036009]

Keywords: poly(3-hexylthiophene-2.5-diyl); graphene; molybdenum disulfide; laser ablation; thin films; optical properties; transmission electron microscope; photodetector

Paper 23073G received Jun. 28, 2023; revised Jul. 22, 2023; accepted Jul. 24, 2023; published Aug. 16, 2023.

1 Introduction

Optical sensors, a category of optical units that measure photovoltaic energy through converting falling light into currents or voltages, are extensively used as an essential part of spectroscopy, imaging, biological science, and night vision.[1–6] Photovoltaic devices can almost be categorized as large-scale broadband or selective selectors, such as Si and InGaAs, which respond to energy powered photons higher than their difference gaps.[7,8] Selective photodetectors, also known as

*Address all correspondence to Amer Al-Nafiey, amer76z@yahoo.com

1934-2608/2023/$28.00

narrowband photodetectors, are designed to detect light at a specific wavelength and generally are applied for biomedical imaging and safety surveillance.[9] Both broadband and selective properties are required to build optical detectors, which show a good optical response to a broad spectrum and are still spectrally distinctive.

Porous silicon (PSi) is a material characterized by its nanoporous to macroporous structure and large surface area. It can be produced from both n-type and p-type silicon using chemical or electrochemical methods. One of the simple techniques used to create PSi is by immersing a Si wafer anode and a gold cathode in an electrolyte containing hydrofluoric (HF) acid. This process is often carried out with a constant current source to maintain a stable concentration of HF, which helps in achieving a more uniform and homogeneous porosity layer.[10] In this method, lasers or intense light are employed as a photon source to generate the required holes in the illuminated section of the silicon wafer, thus initiating the etching process. The silicon wafer functions as the anode in this technique, while materials, such as gold or other conductive substances, that are resistant to HF acid are used as the cathode. To withstand the highly corrosive nature of HF, the electrolysis cell is typically constructed using acid-resistant polymers like Teflon.[11] PSi has a direct band gap, variable refractive index, low reflectivity, as well as indiscriminate morphological installation, which made it a potential substance for the application of photovoltaic.[12] The family of transition metal dichalcogenides (TMDs) has generated considerable interest in the realm of two-dimensional (2D) materials, as evidenced by the existing literature.[13] TMDs possess a hexagonal lattice structure and exhibit light absorption capabilities within the visible-to-infrared range.[14] Due to their exceptionally thin structures, they offer great potential as semiconducting materials. Their advantages include enhanced carrier confinement, electrostatic gate control, and programmable bandgaps, as well as the absence of surface dangling bonds.[13] Consequently, the study of TMD materials, such as molybdenum disulfide (MoS_2), remains an active and dynamic area of research across materials science, physics, and engineering, holding implications for a wide range of fields.[15]

MoS_2 nanoparticles have been synthesized using various techniques and employed as a photodetector in a number of studies. Yin et al.[16] utilized the mechanical exfoliation method to prepare a single-layer phototransistor, which exhibited a responsivity of 7.5 mA/W at a wavelength of 750 nm. In addition, Han et al.[17] developed a MoS_2 photodetector with a responsivity (R) of 1.4×10^5 A/W and a specific detectivity (D) of 9×10^{15} Jones, which were significantly higher than those of Si and Ge photodetectors. On the other hand, Kumar et al.[18] fabricated an efficient UV photodetector using MoS_2 layers and pulsed laser deposition technology, with a specific detectivity (D) of 1.8×10^{14} Jones. Furthermore, Li et al.[19] described a waveguide-integrated MoS_2 photodetector capable of hot-electron-assisted photodetection in the telecom band, exhibiting a responsiveness of 15.7 mA W^{-1} at a wavelength of 1550 nm.

On the other hand, graphene is a 2D material comprising a hexagonal lattice structure of carbon atoms. Its exceptional properties, such as high mechanical strength, large surface area to volume ratio, and high electrical and thermal conductivity, have earned it the title of a "wonder material." Additionally, its transparency and flexibility make it a versatile material suitable for a wide range of applications, including electronics, sensors, energy storage, and biomedical devices.[20] The first graphene photodetector was introduced by Sun et al.,[21] with a photoresponsivity of 0.5 mA/W. Furthermore, Huang et al.[22] discovered that the graphene/HfO/Si photodetector exhibits a significantly greater interfacial gating effect than the graphene/SiO/Si photodetector. The photoresponsivity of the graphene/HfO/Si photodetector is 45.8 A/W. Moreover, Shih et al.[23] demonstrated a practical approach for enhancing surface homogeneity and improving photodetector performance. The PVA/rGO photodetector has an on/off ratio that is 3.5 times higher than that of the rGO photodetector.

Moreover, poly(3-hexylthiophene-2,5-diyl) (P_3HT) is a semiconducting polymer known for its exceptional electronic and optical properties, positioning it as a promising material for various electronic and optoelectronic applications. Its noteworthy features include high charge carrier mobility, solution process ability, and cost-effectiveness, making it an appealing alternative to conventional inorganic semiconductors.[24] In one application, P_3HT was utilized in conjunction with graphene as a photodetector using the spin-coating method. The resulting device demonstrated a responsivity of 0.25 W/A and a specific detectivity of 1.8×10^8 Jones.[25]

Additionally, various fabrication methods can be employed to create these nanomaterials, with one such method being pulse laser ablation (PLA). PLA is particularly noteworthy for its capability to generate nanoparticles with precise control over their size, shape, and narrow size distribution. What sets PLA apart is its avoidance of harmful byproducts, toxic chemicals, or solvents during the synthesis process, making it a safe and environmentally friendly approach for nanomaterial production. As a result, PLA holds promise as a sustainable alternative for producing high-quality nanomaterials.[26]

In this research, the $P_3HT - G/MoS_2$ nanocomposite was prepared by the PLA method for the first time. This nanocomposite was analyzed with different instruments to study the optical, morphological, and electrical properties, and after depositing on the PSi substrate, it was manufactured as a photodetector. Its most important parameters were studied, as well as how changing the number of laser pulses affects the efficiency of the photodetector.

2 Properties of the Detector

Photonic detector convert photons directly into free current carriers, when light falls on the detector the photons exciting the electrons to higher energy levels lead to forming electrical charge carriers (e or h) that remain inside the detector material. The incident photon must has energy equal or greater than band gap energy to excite valence electrons, the longest wavelength that can be absorbing is specific by cut-off wavelength (λ_c) given by the following equation:[27,28]

$$\lambda_0 = \frac{1.24}{E_g(\mathrm{eV})}. \tag{1}$$

These reagents characterized by having a spectral response within a specified range of wavelengths depending on the type of reagent and have a short response time. Therefore, these reagents are preferred over thermal detectors because of their high detectivity, and response time is shorter than thermal reagents and does not require cooling.[27,28] It is an important parameter of the detector that was calculated.

2.1 Responsivity

It is the ratio between the output quantity current or voltage from the detector to the power of the incident radiation. As in the relationship:[27]

$$R = \frac{I_{\text{photocurrent}}}{\mathrm{P}_{\text{input}}}\ (\mathrm{A/W}) \quad \text{or} \quad \frac{V_{\text{photovoltage}}}{\mathrm{P}_{\text{input}}}\ (\mathrm{V/W}). \tag{2}$$

2.2 Quantum Efficiency

It is the ratio between the number of electron–hole pairs generated to the total number of absorbed photons.[29] The quantum efficiency is essentially another way of expressing the effectiveness of the incident optical energy for producing an output of electrical current, it may be related to the responsivity by the following equation:[30]

$$\eta_{\text{quantum}} = R\frac{1.24}{\lambda_{(\mu\mathrm{m})}} \times 100\%. \tag{3}$$

2.3 Detectivity

It is the lowest incident power detected by the detector or is the inverse of the equivalent noise power:[30]

$$D_\lambda = \frac{1}{\mathrm{NEP}} = \frac{R_\lambda}{I_n}\ \mathrm{W}^{-1}. \tag{4}$$

NEP (noise equivalent power) defined, as incident power is required to produce a signal voltage or current equal to the noise voltage or current at the detector output. Detectivity increases when NEP decreases:[31]

$$\mathrm{NEP} = \frac{I_n}{R_\lambda}\mathrm{W}, \tag{5}$$

where I_n is the total noise current.

The term detectivity replaced by specific detectivity (D^*) used to compare types of reagents and is known by relationship:[31]

$$D^* = R_\lambda \frac{\sqrt{A.\Delta f}}{I_n}\ \mathrm{cm\,HZ^{1/2}\,W^{-1}}, \tag{6}$$

$$I_n = (2qI_d\Delta f)^{1/2}, \tag{7}$$

Δf is the bandwidth, A is the active area of the detector, I_d is the dark current, and q is the electron charge.

3 Materials

Graphite target [(99.99% quality) molecular weight (12.01 g/mol)] and MoS_2 target [(99.99% quality) molecular weight (160.07 g/mol)], with diameters (2 cm) and thickness (4 mm), were purchased from Shenzhen Rearth Technology Co. Limited, China. Also P_3HT polymer powder with molecular weight 16,000 g/mol was purchased from Shenzhen Rearth Technology Co. Limited, China.

3.1 Experimental

This section summarized the steps to fabricate ($P_3HT - G/MoS_2$) thin films and PSi.

3.2 Preparation of $P_3HT - G/MoS_2$ Nanocomposite Using the Laser Ablation Method

Graphite and MoS_2 targets are cleaned with methanol to remove suspended impurities. A P_3HT semiconducting polymer is prepared by dissolving 0.5 mg of P_3HT powder in 40 mL of chloroform solution under a magnetic stirrer for 30 min. The graphite target is placed in a clean beaker, and 5 mL of the P_3HT polymer is placed on top and ablated with a laser (Q-switch Nd-YAG) ($\lambda = 1064$ nm) ($E_{\mathrm{pulse}} = 200$ mJ/pulse), (pulse = 200) and the repetition rate is 1 Hz. A MoS_2 target was placed in the graphene colloidal nanosolution and ablated with the same laser parameters as above. These previous steps are repeated but with a different number of pulses 500 and 800 pulse for both graphite and MoS_2. Figure 1 shows a sketch of the main phases of pulsed laser ablation in liquid (PLAL) technique.

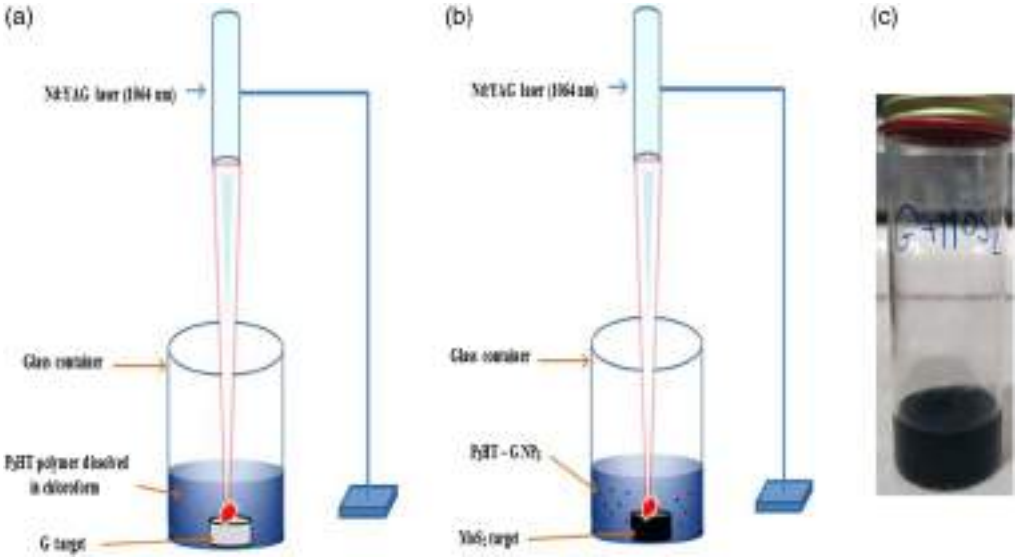

Fig. 1 Diagram of the main stages of PLAL technique: (a) graphite target placed in P_3HT polymer solution. (b) Placing a target of MoS_2 in a colloidal nanosolution of P_3HT – graphene. (c) Photograph of the nanocomposite P_3HT – graphene/MoS_2.

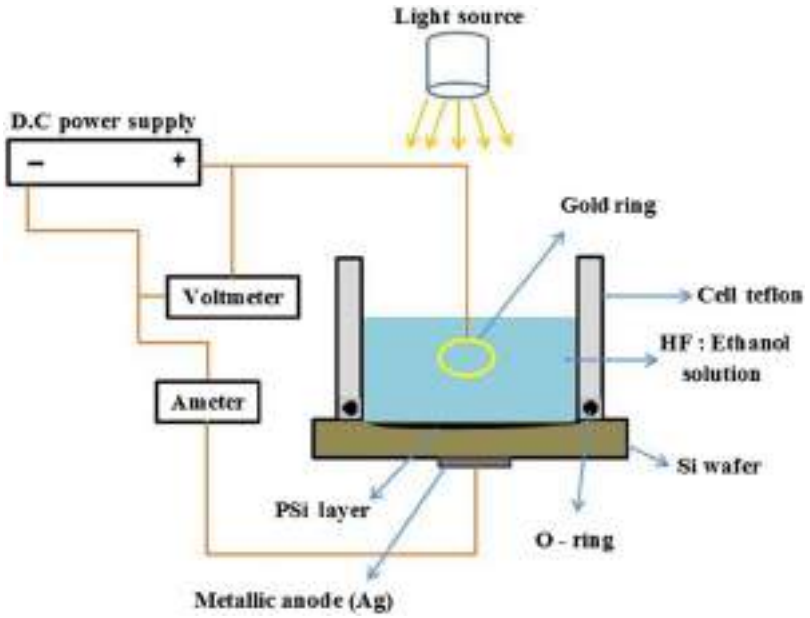

Fig. 2 Schematic diagrams of electrochemical etching setup.

3.3 Preparation of Porous Silicon Substrate

PSi layers were prepared by anodic etching with an electrochemical cell, in which a substrate with an etched area of 0.785 cm^2 was etched in the Teflon etch cell using a 1:1 mixture of ethanol purity 99.99% and aqueous hydrogen fluoride 50% purity. The sample was anodized at a current density of 15 mA/cm^2; for 15 min etch time, a thin layer of silver was deposited on the reverse side. Without further heat or chemical treatment, it was made after engraving. Figure 2 shows schematic diagrams of the electrochemical etch setup. This device was prepared and worked on in the laboratories of the College of Science/Al-Mustansiriya University.

3.4 Preparation Heterojunction Photodetector

The colloidal $P_3HT - G/MoS_2$ nanoparticles prepared with different laser pulses are shown in Fig. 3. It is extracted from the solution with a pipette and then only five drops are dropped on the PSi surface at 40°C and when it dries another five drops are added and the process is repeated three times then the film is ready. This device was prepared and worked on in the laboratories of the College of Science/Al-Mustansiriya University. In addition, silver paste was placed on the $P_3HT - G/MoS_2$ thin films to measure electrical properties. Photodetector devices are manufactured in with the following architecture:

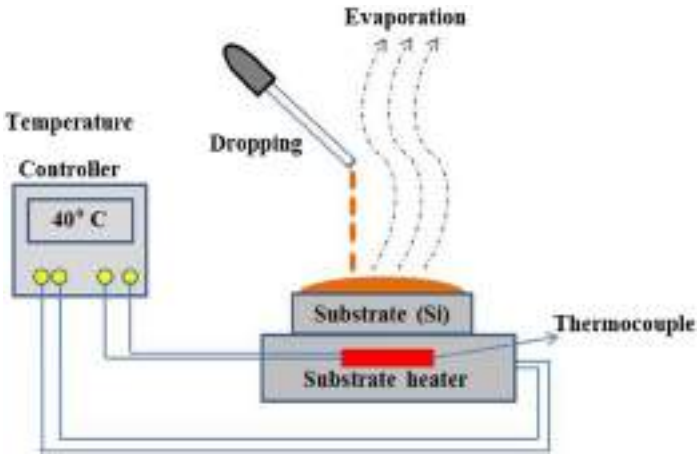

Fig. 3 Diagram drop casting method.

$$\text{Ag} \rightarrow \text{PSi} \rightarrow \text{active layer}(P_3HT - G/MoS_2) \rightarrow \text{Ag}.$$

4 Results and Discussion

4.1 Optical Properties of $P_3HT - G/MoS_2$ Thin Films

Figure 4 shows the absorption spectra for each P_3HT, G, and MoS_2 in the chloroform solution, where it was observed that the absorption peak of the P_3HT polymer is in the visible region at a wavelength of 446 nm and was in agreement with the report.[32] Meanwhile the graphene in the ultraviolet at 271 nm, consistent with previous studies[33] and MoS_2 at 264 nm, and this is identical to the report.[34] The combination of these three materials leads to the formation of a new nanocomposite with a broad absorption range extending from UV-NIR, and this will be very useful in optoelectronics. It shows very promising properties not only for future nanoscale applications but also for photonic applications, such as solar cells and photodetectors.

The absorption spectra of all prepared samples are shown in Fig. 5. The absorption spectrum of a nanocomposite $P_3HT/G/MoS_2$. The absorption band around 271 nm increases with the

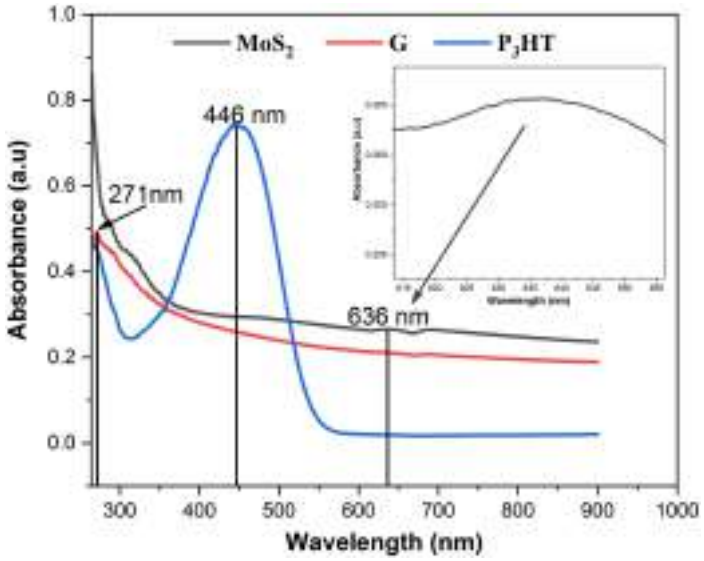

Fig. 4 Absorbance spectra of G and MoS_2.

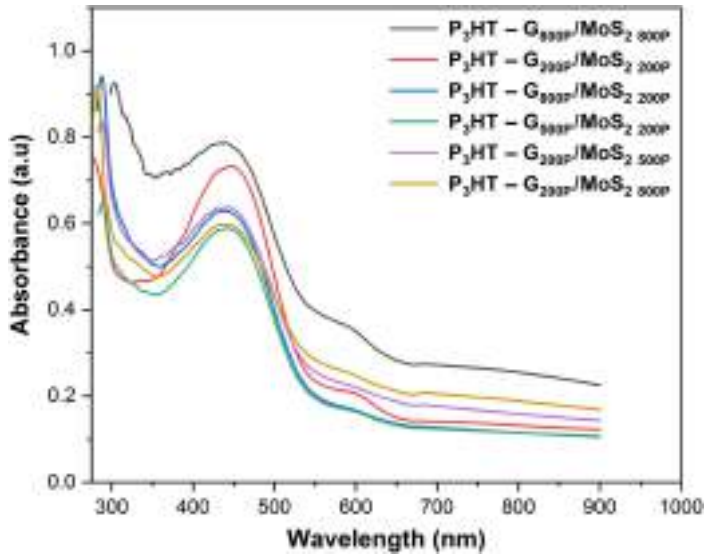

Fig. 5 Absorbance spectra of all and P_3HT prepared in chloroform solution: the prepared samples.

Table 1 Absorption values for all the prepared samples.

	G		MoS_2	
Sample	Absorbance (a.u.)	λ_{peak} (nm)	Absorbance (a.u.)	λ_{peak} (nm)
$P_3HT - G_{200P}/MoS_{2\,200P}$	0.74	277	0.20	595
$P_3HT - G_{200P}/MoS_{2\,500P}$	0.83	289	0.24	601
$P_3HT - G_{200P}/MoS_{2\,800P}$	0.92	282	0.21	600
$P_3HT - G_{500P}/MoS_{2\,200P}$	0.64	290	0.16	591
$P_3HT - G_{800P}/MoS_{2\,200P}$	0.94	293	0.16	591
$P_3HT - G_{800P}/MoS_{2\,800P}$	0.92	303	0.34	606

incorporation of graphene into MoS_2, which may be attributed to the blackbody properties of graphene. Also seen is that increasing the number of laser pulses for both graphene and MoS_2 can increase absorption due to an increase in nanoparticle concentration. Table 1 shows the absorption spectra for all the prepared samples.

The photon energy (E_g) was calculated for MoS_2, G, and P_3HT nanoparticles as a function of $(\alpha hv)^{1/2}$ as shown in Figs. 6(a)–6(c), where they were on the form of colloidal suspension in chloroform solution.

Figures 7(a)–7(c) shows the photon energy (E_g) for $P_3HT - G/MoS_2$ nanocomposite as a function of $(\alpha hv)^{1/2}$, whereas colloidal suspension in chloroform solution. α is the absorption coefficient. The energy gap values of the $P_3HT - G/MoS_2$ compound decreased from about 2.03 to 1.87 eV with increasing number of laser ablation pulses for both the graphene and MoS_2 target. This decrease in the energy gap is attributed to the increase in graphene and its combination with MoS_2 leads to a decrease in the band gap because of the improved electrical conductivity of hybrid material,[35] or due to the creation of defects in the material by breaking the

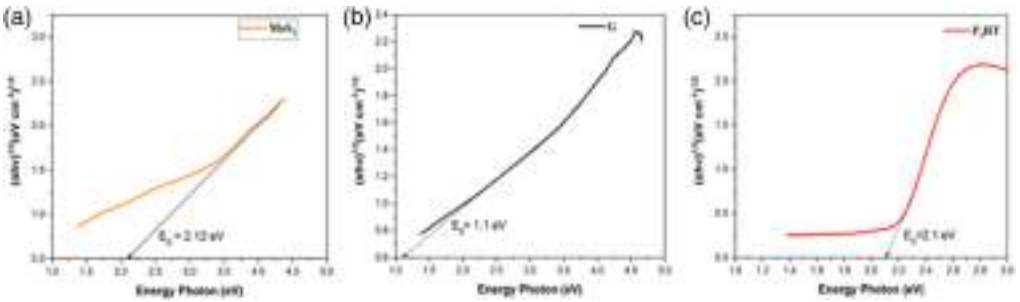

Fig. 6 (a)–(c) The allowed indirect optical energy gap for MoS_2, G, and P_3HT nanoparticles in the chloroform solution.

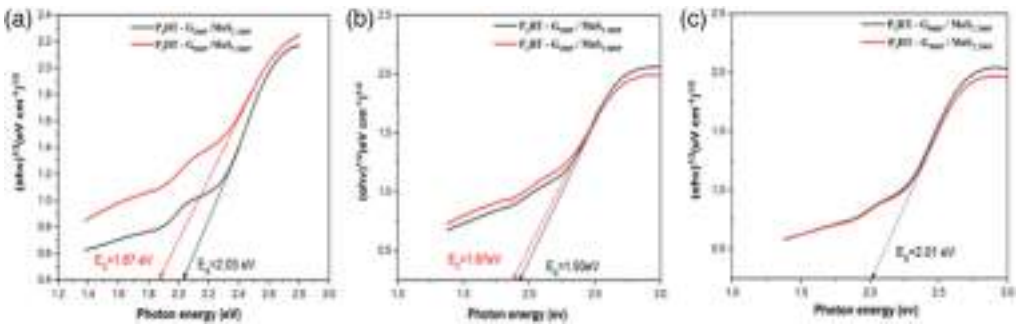

Fig. 7 (a)–(c) The photon energy (E_g) of prepared samples as a function of the $(\alpha hv)^{1/2}$.

Table 2 Energy gap and absorption coefficient values for MoS_2, G, and P_3HT for all prepared samples.

Sample	Allowed indirect E_g (eV)	The absorption coefficient α (cm^{-1})
MoS_2	2.1	0.61
G	1.1	0.43
P_3HT	2.1	0.05
$P_3HT - G_{200P}/MoS_{2\,200P}$	2.03	0.45
$P_3HT - G_{200P}/MoS_{2\,500P}$	1.93	0.44
$P_3HT - G_{200P}/MoS_{2\,800P}$	1.87	0.47
$P_3HT - G_{500P}/MoS_{2\,200P}$	2.01	0.35
$P_3HT - G_{800P}/MoS_{2\,200P}$	2.01	0.35
$P_3HT - G_{800P}/MoS_{2\,800P}$	1.87	0.63

Mo–S bonds and creating sulfur vacancies. These defects act as trap states for electrons and holes, reducing the bandgap of the material. The number of defects increases with the number of laser ablation pulses, which results in a decrease in the energy gap of the material. This effect has been observed in several studies, including a study by Wang et al.[36] and another by Huang et al.[37] The indirect energy gap and absorption coefficient values obtained are shown in Table 2. We note from this table that the highest value of the absorption coefficient is 0.63 cm^{-1}, which is due to the sample $P_3HT - G_{800P}/MoS_{2\,800P}$, as the reason for the increase in the absorption coefficient is the result of an increase in the concentration of nanoparticles for both graphene and MoS_2, which leads to an increase in absorbance

4.2 Morphological Characteristics

Transmission electron microscope (TEM) used to analyze the morphological aspects of the nanocomposites. Figures 8–13 show 50 nm scale TEM images of the $P_3HT - G/MoS_2$ nanocomposite with different laser pulses in graphene as well as for MoS_2 and that the shape of the nanoparticles is hemispherical. On the other hand, we note the accumulation of these

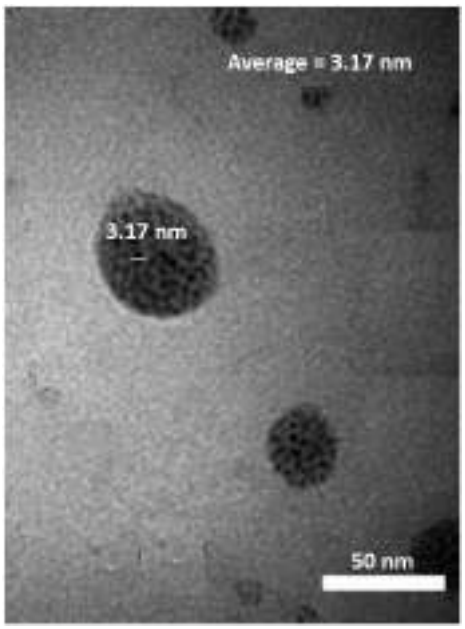

Fig. 8 TEM image of $P_3HT - G(200P)/MoS_2(200P)$ colloidal.

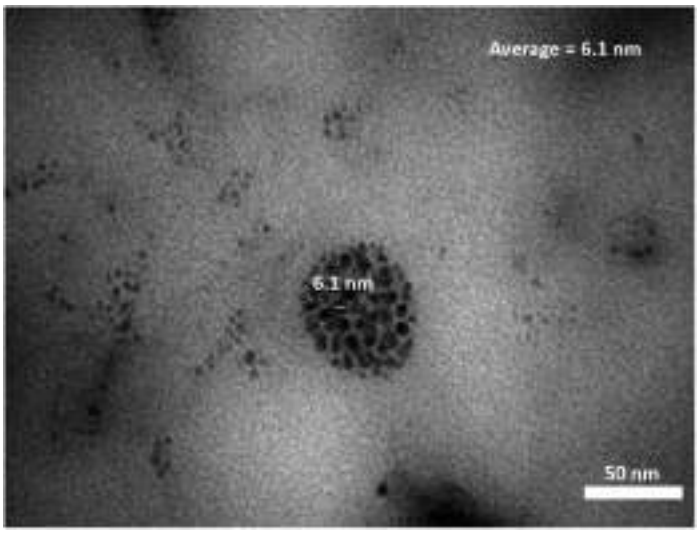

Fig. 9 TEM image of $P_3HT - G(200P)/MoS_2(500P)$ colloidal nanoparticles.

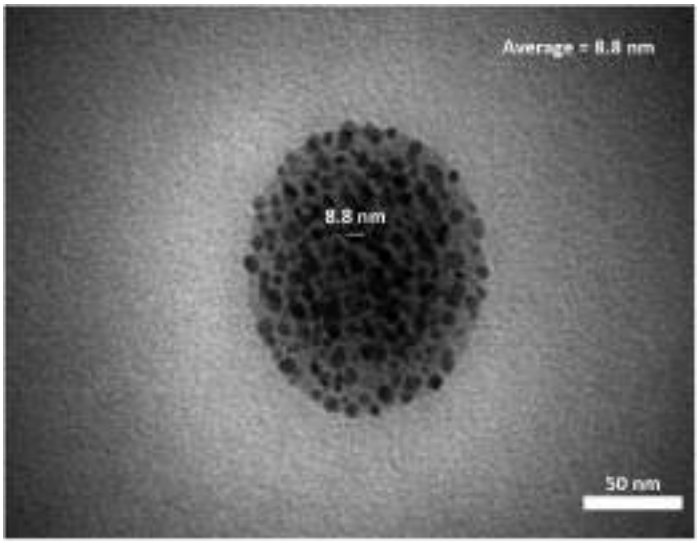

Fig. 10 TEM image of $P_3HT - G(200P)/MoS_2(800P)$ colloidal.

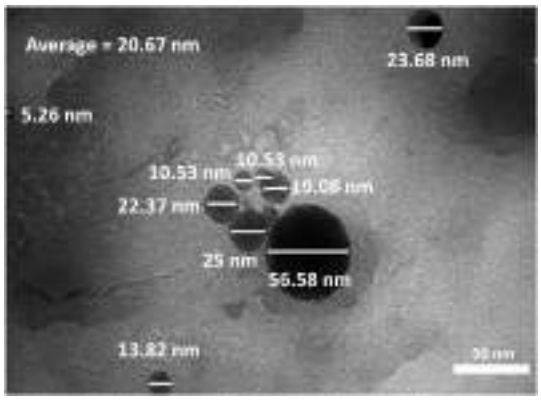

Fig. 11 TEM image of P3HT – G(500P)/MoS2(200P) colloidal nanoparticles.

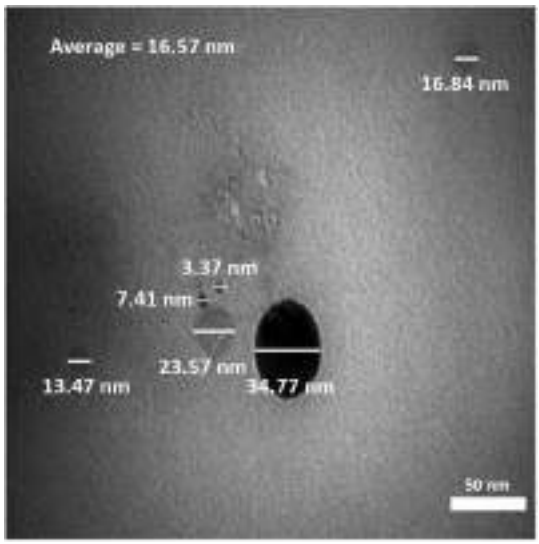

Fig. 12 TEM image of $P_3HT - G(800P)/MoS_2(200P)$ colloidal.

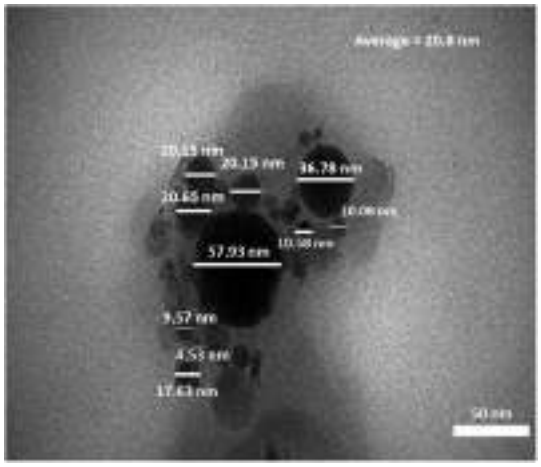

Fig. 13 EM image of $P_3HT - G(800P)/MoS_2(800P)$ colloidal nanoparticles.

nanoparticles to form a large spherical nanoparticle. The average size of the nanoparticles is between 3.1 and 20.8 nm, depending on the number of laser pulses.

4.3 Electrical Properties of the Heterojunction

4.3.1 *Dark current–voltage measurements of photodetector*

The electrical behavior of $Ag/PSi/P_3HT - G/MoS_2/Ag$ as a Schottky or heterojunction is generally determined as a function of the current–voltage characteristics. We can see in Figs. 14(a)–14(f) that at voltages below 1 V, the forward current is quite little. Due to the presence of recombination centers, which only happens at low voltages, this current is known as the recombination current. The built-in potential and the width of the depletion layer are reduced as the bias voltage value is increased on both sides of the heterojunction. At high voltage, an exponential current known as diffusion current emerges and grows with rising bias voltage. In this location, polarization, which can produce voltage, can give electrons enough energy to cross the barrier separating the junction's two sides. It has two areas when reverse biased, the first of which the current is plainly visible at low levels of the reverse voltage due to a decrease in the concentration of carriers and an expansion of the depletion region's breadth. Diffusion current predominates in the second range at high-voltage until saturation.[37,38] The behavior of the current as a function of

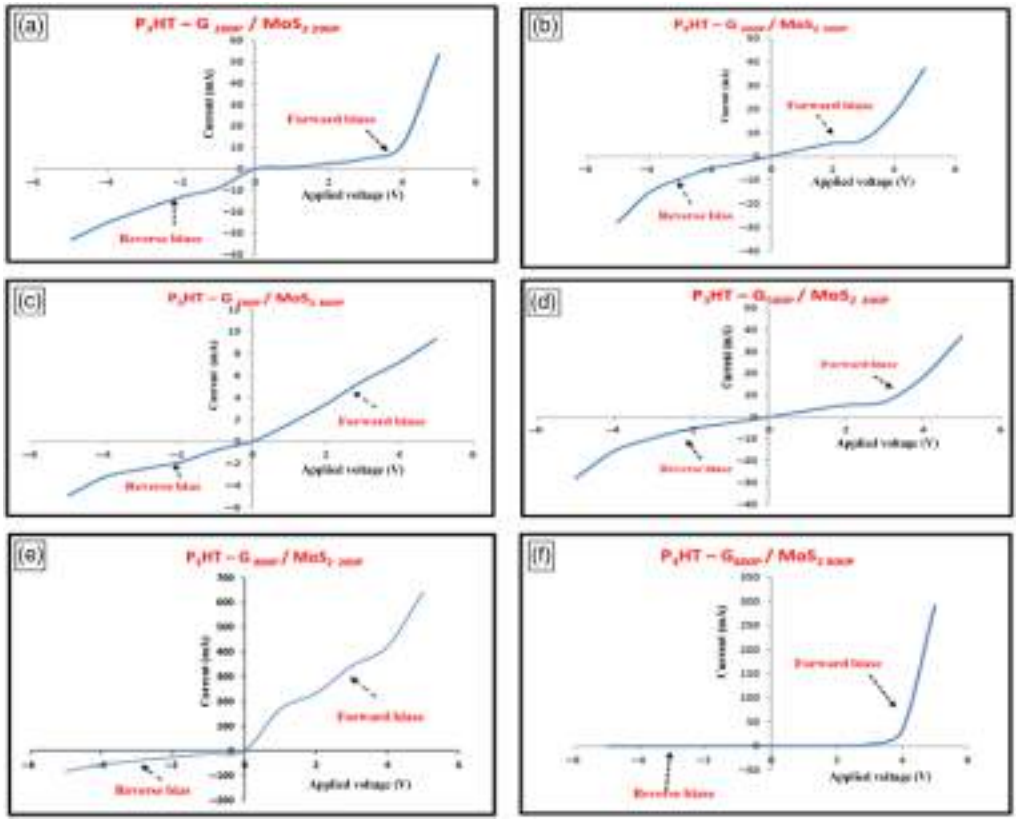

Fig. 14 (a)–(f). Dark ($I - V$) characteristic of $Ag/PSi/P_3HT - G/MoS_2/Ag$ at the number different laser pulses.

voltage is Schottky, as was already noted. This means that the forward current behaves similarly to the reverse current for a variety of reasons, one of which being the material's high resistance. The network's short lifespan or nonconformity. The electrical behavior of $Ag/PSi/P_3HT - G/MoS_2/Ag$ is that of a forward-biased diode and the forward current value at bias is very tiny, as shown in Fig. 14(f). The voltage is below 3 V.

4.3.2 *Photodetector characteristics*

In photodetector applications, photodetectors properties, including spectrum responsiveness, spectral detectivity, quantitative efficiency, and longevity, are crucial. The production of photonic devices can be successful with these parameters.

Spectral Responsivity (R_λ). Equation (2) was used to determine the spectral responsivity of structures in the 350 to 1000 nm wavelength range at a 3 V bias voltage. Three heterojunctions make up the $Ag/PSi/P_3HT - G/MoS_2/Ag$ structure. $Ag/PSi/P_3HT - G/MoS_2/Ag$ have three depletion regions because the first heterojunction is between the Ag layer and the PSi (Ag/PSi), the second heterojunction is between the PSi layer and the $P_3HT - G/MoS_2$ thin film, and the third heterojunction is between the $P_3HT - G/MoS_2$ thin film and Ag layer.

Plots of the spectrum response versus wavelength for the $Ag/PSi/P_3HT - G/MoS_2/Ag$ structure created using various laser pulses are shown in Figs. 15(a)–15(f). The figures demonstrate that the spectral response curve of $Ag/PSi/P_3HT - G/MoS_2/Ag$ has numerous response peaks, with the highest peak occurring at 900 nm and being caused by the silicon's absorption edge, in line with earlier research.[9] Due to the $P_3HT - G/MoS_2$ nanoparticles' absorption edge, the peak is at 760 nm. From the calculations, it was shown that the $Ag/PSi/P_3HT - G_{200P}/MoS_{2\,800P}/Ag$ sample's $Ag/PSi/P_3HT - G_{800P}/MoS_{2\,800P}/Ag$ sample's spectral sensitivity of the silicon absorption edge rises by 0.05 A/W at a wavelength of 850 nm and by 0.35 A/W at a wavelength of 900 nm.

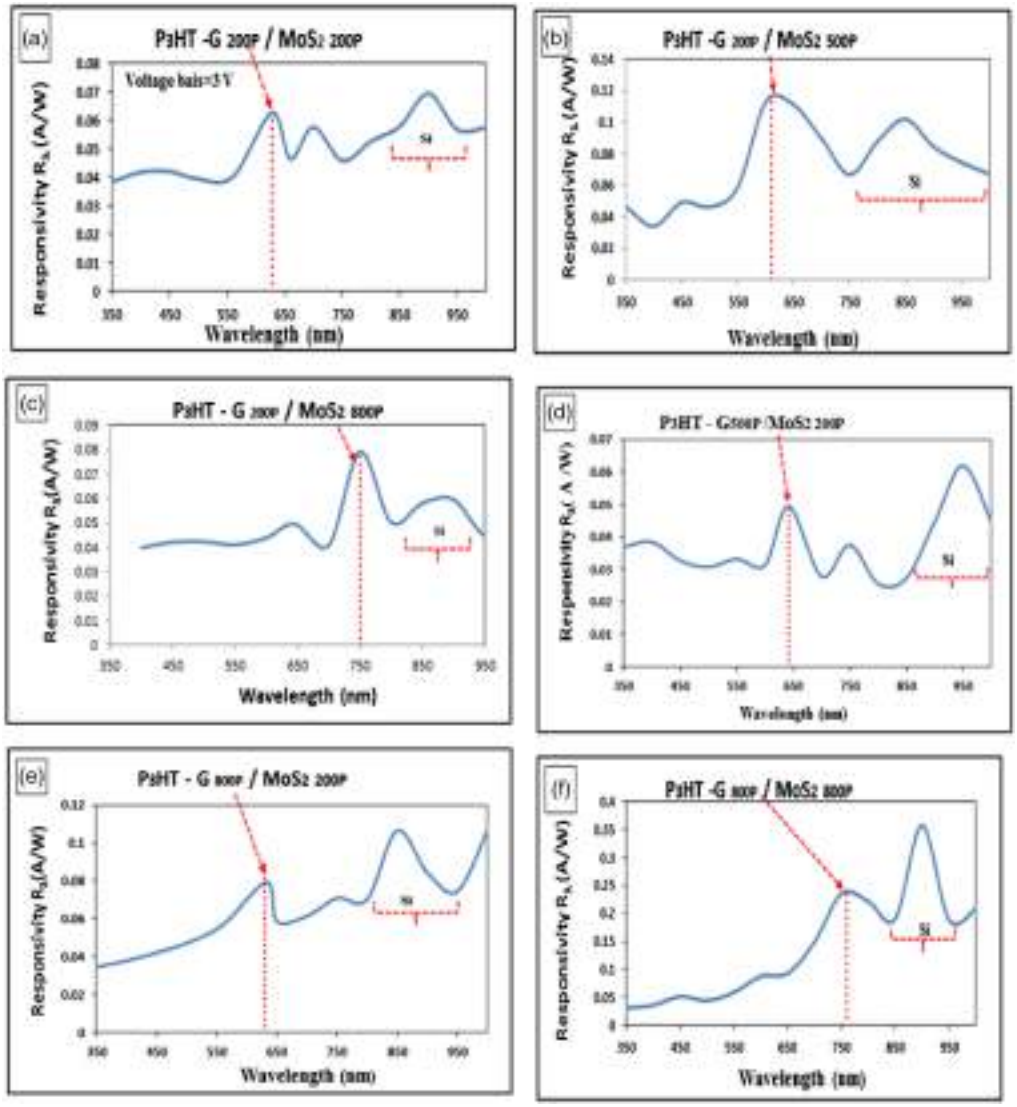

Fig. 15 (a)–(f) Responsivity as a function of wavelength of $Ag/PSi/P_3HT - G/MoS_2/Ag$ photodetectors at different laser pulses.

According to the results, the $P_3HT - G/MoS_2$ film may absorb light with a greater energy, such as that between 650 and 750 nm, whereas light with a lower energy, such as that between 800 and 950 nm, can totally affect the Si substrate. The absorption edges of $P_3HT - G/MoS_2$ and PSi are responsible for these outcomes. Due to the $P_3HT - G/MoS_2$ nanoparticles' absorption edge, the $Ag/PSi/P_3HT - G/MoS_2/Ag$ photodetectors responsiveness rises from 0.062 to over 0.23 A/W. Increased light absorption, expanded depletion breadth and length, and decreased dark current are all responsible for this improvement.

Specific detectivity (D).* From Figs. 16(a)–16(f), it was observed that the specific detectivity of the silicon absorption edge of 8.3×10^{11} cm $Hz^{1/2}$ W^{-1} increases at a wavelength of 850 nm for the sample $Ag/PSi/P_3HT - G_{200P}/MoS_{2\,800P}/Ag$ up to 5.1×10^{12} cm $Hz^{1/2}$ W^{-1} at a wavelength of 900 nm for the sample $Ag/PSi/P_3HT - G_{800P}/MoS_{2\,800P}/Ag$. The specific detectivity is one of the crucial photodetectors metrics, and as such, it serves as a benchmark for the lowest detectable performance. The specific detectivity for the $Ag/PSi/P_3HT$ and $G/MoS_2/Ag$ photodetectors, respectively, in various laser pulses, is depicted as a function of wavelength in Figs. 16(a)–16(f).

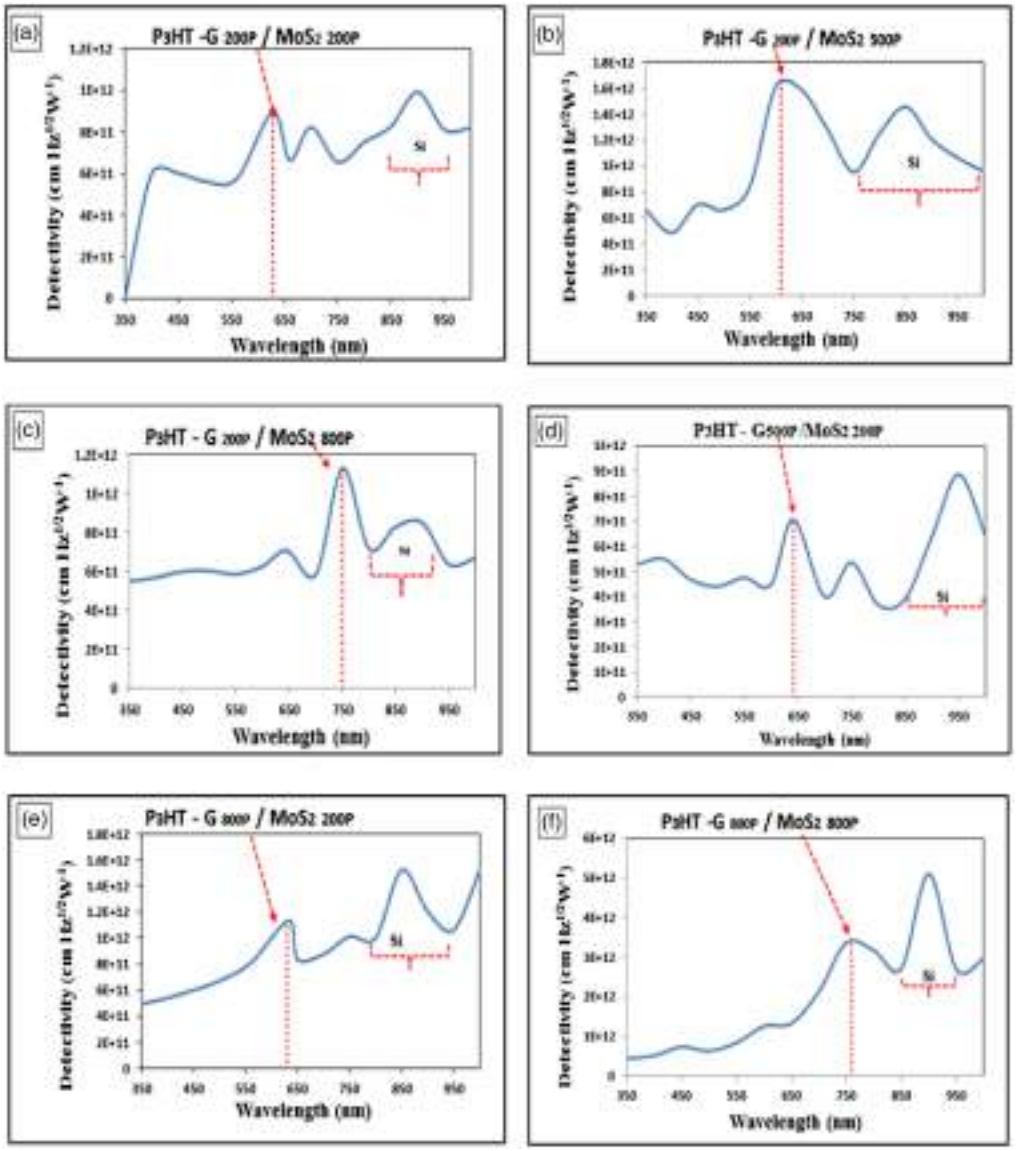

Fig. 16 (a)–(f) Spectral detectivity plots for $Ag/PSi/P_3HT - G/MoS_2/Ag$ photodetectors at different laser pulses.

These figures demonstrate the correlation between responsiveness and recognizing ability. The maximal $D*$ for the photodetectors $Ag/PSi/P_3HT - G_{800P}/MoS_{2\,800P}/Ag$ was determined to be 3.3×10^{12} W^{-1} cm $Hz^{1/2}$.

Quantum efficiency. Figures 17(a)–17(f) depict the $Ag/PSi/P_3HT - G/MoS_2/Ag$ structure's quantum efficiency as a function of wavelength 350 to 1000 nm. According to the data we gathered, the greatest peak quantum efficiency for $Ag/PSi/P_3HT - G_{800P}/MoS_{2\,800P}/Ag$ was 38.9% at 760 nm. This is because there is more absorption in this area, which causes more carriers to be generated in the depletion zone, increasing spectrum sensitivity and, ultimately, quantum efficiency. The detector parameter findings for $Ag/PSi/P_3HT - G/MoS_2/Ag$ in various laser pulses are shown in Table 3. According to the data, the quantum efficiency of the silicon absorption edge improves from 8% for the $Ag/PSi/P_3HT - G_{200P}/MoS_{2\,800P}/Ag$ sample at 850 nm to 49.2% for the $Ag/PSi/P_3HT - G_{800P}/MoS_{2\,800P}/Ag$ sample at 900 nm. Table 4 lists the specifications for all the films created and for the silicon absorption edge photodetectors that have been improved by the $P_3HT - G/MoS_2$ nanocomposite.

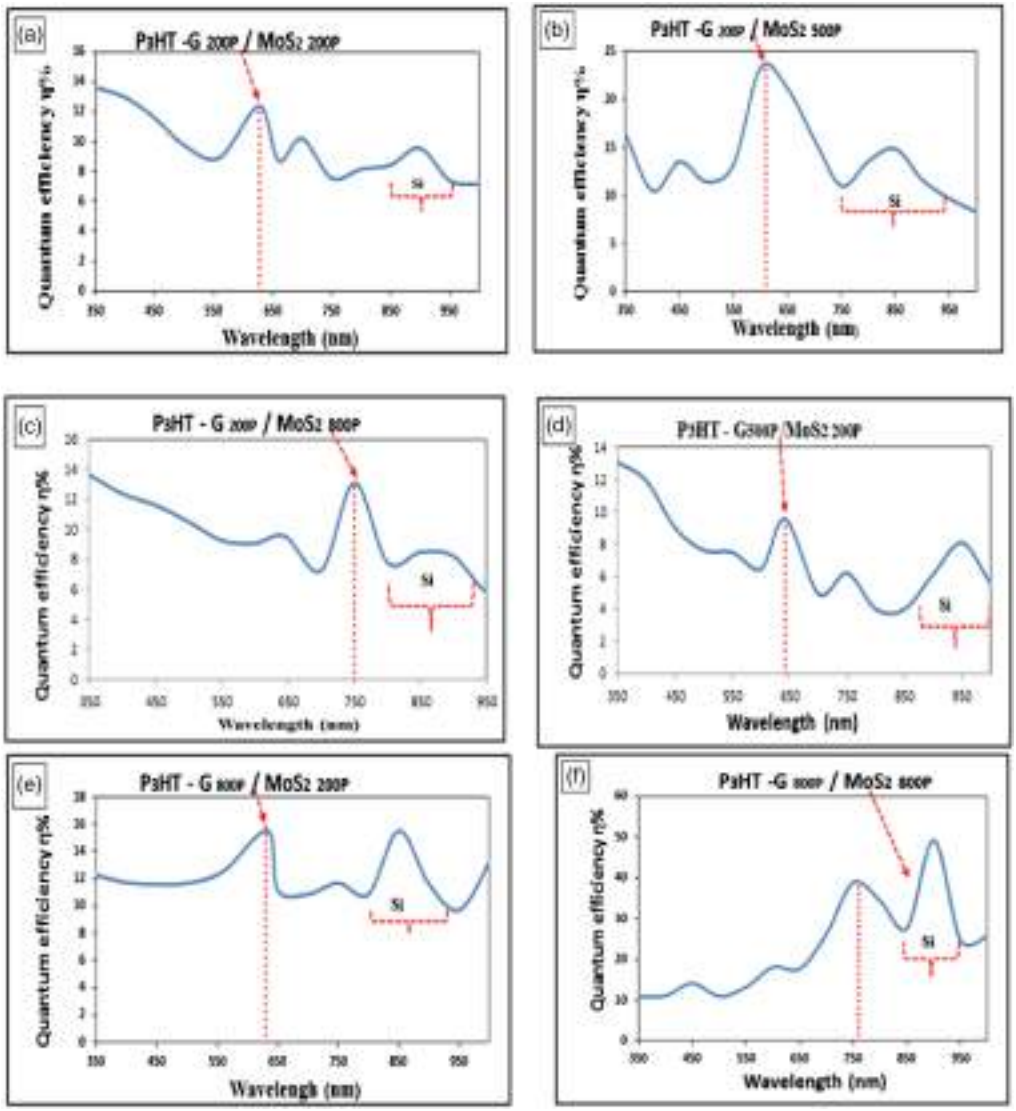

Fig. 17 (a)–(f) Quantum efficiency for $Ag/PSi/P_3HT - G/MoS_2/Ag$ photodetectors at different laser pulses.

Table 3 Photodetector parameters to the absorption edge of $P_3HT - G/MoS_2$ nanoparticles for all the films prepared.

Heterojunction (photodetectors)	Wavelength (nm)	Responsivity specific $R\lambda$ (A/W)	Detectivity specific D^* (cm $Hz^{1/2}$ W^{-1})	Quantum efficiency η%
$Ag/PSi//P_3HT - G_{200P}/MoS_{2\,200P}/Ag$	628	0.062	8.95×10^{11}	12.3
$Ag/PSi/P_3HT - G_{200P}/MoS_{2\,500P}/Ag$	600	0.11	1.61×10^{12}	23.3
$Ag/PSi/P_3HT - G_{200P}/MoS_{2\,800P}/Ag$	750	0.07	1.13×10^{12}	13.0
$Ag/PSi/P_3HT - G_{500P}/MoS_{2\,200P}/Ag$	633	0.07	1.13×10^{12}	15.5
$Ag/PSi/P_3HT - G_{800P}/MoS_{2\,200P}/Ag$	642	0.04	7.0×10^{11}	9.5
$Ag/PSi/P_3HT - G_{800P}/MoS_{2\,800P}/Ag$	760	0.23	3.3×10^{12}	38.9

Table 4 Parameters of the photodetectors of the silicon absorption edge enhanced by $P_3HT - G/MoS_2$ nanocomposite and for all prepared films.

Heterojunction (photodetectors)	Wavelength (nm)	Responsivity specific $R\lambda$ (A/W)	Detectivity specific D^* ($cm\,Hz^{1/2}\,W^{-1}$)	Quantum efficiency η%
$Ag/PSi//P_3HT - G_{200P}/MoS_{2\,200P}/Ag$	900	0.06	9.9×10^{11}	9.5
$Ag/PSi/P_3HT - G_{200P}/MoS_{2\,500P}/Ag$	850	0.10	1.4×10^{12}	14.8
$Ag/PSi/P_3HT - G_{200P}/MoS_{2\,800P}/Ag$	850	0.05	8.3×10^{11}	8.0
$Ag/PSi/P_3HT - G_{500P}/MoS_{2\,200P}/Ag$	850	0.10	1.5×10^{12}	15.5
$Ag/PSi/P_3HT - G_{800P}/MoS_{2\,200P}/Ag$	950	0.06	8.8×10^{11}	8
$Ag/PSi/P_3HT - G_{800P}/MoS_{2\,800P}/Ag$	900	0.35	5.1×10^{12}	49.2

5 Conclusions

$Ag/PSi/P_3HT - G/MoS_2/Ag$ heterojunction photodetectors have been fabricated by drop casting method that has been used to deposit a $P_3HT - G/MoS_2$ nanoparticles on PSi and prepared for the first time by the method of laser ablation. $P3HT - G/MoS_2$ shows a sufficient absorbance in the range of specter UV–visible. Through the results of the photodetector parameters, we notice that with an increase in the number of laser ablation pulses for both the graphene and MoS_2 target, the responsivity specific, detectivity specific, and quantum efficiency will increase, as the responsivity specific increases from 0.04 A/W at 642 nm, which belong to the sample $Ag/PSi//P_3HT - G_{200P}/MoS_{2\,200P}/Ag$ to 0.23 A/W at 760 nm, which belong to the sample $Ag/PSi/P_3HT - G_{800P}/MoS_{2\,800P}/Ag$, the detectivity specific increases from 7.0×10^{11} $cm\,Hz^{1/2}\,W^{-1}$ at 600 nm, which belong to the sample $Ag/PSi//P_3HT - G_{200P}/MoS_{2\,200P}/Ag$ to 3.3×10^{12} $cm\,Hz^{1/2}\,W^{-1}$ at 760 nm, which belong to the sample $Ag/PSi/P_3HT - G_{800P}/MoS_{2\,800P}/Ag$ and the quantum efficiency increases from 9.5% at 642 nm, which belong to the sample $Ag/PSi//P_3HT - G_{200P}/MoS_{2\,200P}/Ag$ to 38.9% at 760 nm, which belong to the sample $Ag/PSi/P_3HT - G_{800P}/MoS_{2\,800P}/Ag$. On the other hand, the responsivity specific, detectivity specific, and quantum efficiency of the silicon absorption edge will increase with an increase in number of laser ablation pulses for both the graphene and MoS_2 target, as a result of the deposition of $P_3HT - G/MoS_2$ nanocompositions, which worked to improve the characteristics of the photodetector. The highest responsivity specific, detectivity specific, and quantum efficiency around 0.35 A/W, 5.1×10^{12} $cm\,Hz^{1/2}\,W^{-1}$, and 49.2%, respectively, at 900 nm, which belong to the sample $Ag/PSi/P_3HT - G_{800P}/MoS_{2\,800P}/Ag$. This indicates that sample $Ag/PSi/P_3HT - G_{800P}/MoS_{2\,800P}/Ag$ is the best concentration of nanocomposite as a reagent and also as an enhancer for silicon nanowires photodetector.

Data Availability Statement

All data supporting the findings of this study are available within the article. The code and materials used in this research are also available upon request. Contact the corresponding author for further information.

References

1. B. Ghosh et al., "Fabrication of the SnS/ZnO heterojunction for PV applications using electrodeposited ZnO films," *Semicond. Sci. Technol.* **24**(2), 025024 (2009).
2. A. N. Abd, M. Abdulridha Wasna'a, and M. O. Dawood, "Effect of SnS thin film on the performance of porous silicon photodiode," *Int. Lett. Chem. Phys. Astron.* **63**, 67–76 (2016).
3. B. Ghosh et al., "Single-source organometallic chemical vapor deposition of sulfide thin films," *Appl. Surf. Sci.* **257**, 3670 (2011).
4. A. Abd, N. Habubi, and R. A. Ismail, "Preparation of colloidal cadmium selenide nanoparticles by pulsed laser ablation in methanol and toluene," *J. Mater. Sci. Mater. Electron.* **25**, 3190–3194 (2014).
5. N. F. Habubi, R. A. Ismail, and A. N. Abd, "Synethesis and characterization of nano crystalline porous silicon layer for sola cells applications," *Nanosci. Nanotechnol.* **8**, 279–283 (2014).

6. N. F. Habubi et al., "Fabrication and characterization of a p-AgO/PSi/n-Si heterojunction for solar cell applications," *Silicon* **10**, 371–376 (2018).
7. A. M. A. Majeed et al., "Fabrication and characterization of copper oxide nanoparticles/psi heterodiode," *Int. Lett. Chem. Phys. Astron.* **57**, 25 (2015).
8. A. N. Abd et al., "Enhancing the electrical properties of porous silicon photodetector by depositing MWCNTs," *Int. J. Nanoelectron. Mater.* **11**(3), 241–248 (2018).
9. M. H. Hassoni et al., "Invention and description of p-CuO/n-Si (200 °C) heterojunction for photodiode applications," *J. Global Pharma Technol.* **11**(2), 601–606 (2019).
10. A. Uhlir, Jr., "Electrolytic shaping of germanium and silicon," *Bell Syst. Tech. J.* **35**(2), 333–347 (1956).
11. R. S. Dubey, "Electrochemical fabrication of porous silicon structures for solar cells," *Nanosci. Nanoeng.* **1**(1), 36–40 (2013).
12. S. A. Fadaam et al., "Enhanced efficiency of CdTe photovoltaic by thermal evaporation vacuum," *Energy Proc.* **157**, 635–643 (2019).
13. A. Rai et al., "Progress in contact, doping and mobility engineering of MoS_2: an atomically thin 2D semiconductor," *Crystals* **8**(8), 316 (2018).
14. Q. Cui et al., "Material and device architecture engineering toward high performance two-dimensional (2D) photodetectors," *Crystals* **7**(5), 149 (2017).
15. K. M. Freedy and S. J. McDonnell, "Contacts for molybdenum disulfide: interface chemistry and thermal stability," *Materials* **13**(3), 693 (2020).
16. Z. Yin et al., "Single-layer MoS_2 phototransistors," *ACS Nano* **6**(1), 74–80 (2012).
17. P. Han et al., "Highly sensitive MoS_2 photodetectors with graphene contacts," *Nanotechnology* **29**(20), 20LT01 (2018).
18. S. Kumar et al., "High performance UV photodetector based on MoS_2 layers grown by pulsed laser deposition technique," *J. Alloys Compd.* **835**, 155222 (2020).
19. Z. Li et al., "Telecom-band waveguide-integrated MoS_2 photodetector assisted by hot electrons," *ACS Photonics* **9**(1), 282–289 (2022).
20. K. S. Novoselov et al., "Electric field effect in atomically thin carbon films," *Science* **306**(5696), 666–669 (2004).
21. B. Sun et al., "Progress on crystal growth of two-dimensional semiconductors for optoelectronic applications," *Crystals* **8**(6), 252 (2018).
22. Z. Huang et al., "Interfacial gated graphene photodetector with broadband response," *ACS Appl. Mater. Interfaces* **13**(19), 22796–22805 (2021).
23. Y.-S. Shih et al., "Low-power photodetectors based on PVA-modified reduced graphene oxide hybrid solutions," *Macromol. Rapid Commun.* **43**(8), 2100854 (2022).
24. M. Svensson et al., "High-performance polymer solar cells of an alternating polyfluorene copolymer and a fullerene derivative," *Adv. Mater.* **15**(12), 988–991 (2003).
25. A. Yadav et al., "Poly-(3-hexylthiophene)/graphene composite based organic photodetectors: the influence of graphene insertion," *Thin Solid Films* **675**, 128–135 (2019).
26. E. Fazio et al., "Nanoparticles engineering by pulsed laser ablation in liquids: concepts and applications," *Nanomaterials* **10**(11), 2317 (2020).
27. W. Budde, *Physical Detectors of Optical Radiation*, Academic Press (1983).
28. Kirik-Othmer, "Photodetectors," in *Encyclopedia of Chemical Technology*, Vol. **17**, John Wiley & Sons (1982).
29. K. M. Al-Obaidi, M. Ismail, and A. M. A. Rahman, "Passive cooling techniques through reflective and radiative roofs in tropical houses in Southeast Asia: a literature review," *Front. Archit. Res.* **3**(3), 283–297 (2014).
30. L. De Stefano et al., "Milling effects upon quantitative determinations of chrysotile asbestos by the reference intensity ratio method," *Powder Diffraction* **15**(1), 26–29 (2000).
31. Y. An et al., "Characterization of carbon nanotube film-silicon Schottky barrier photodetectors," *J. Vac. Sci. Technol. B* **30**(2), 021805 (2012).
32. M. A. Ansari et al., "Synthesis and characterization of poly (3-hexylthiophene): improvement of regioregularity and energy band gap," *RSC Adv.* **8**(15), 8319–8328 (2018).
33. R. Zhang et al., "Three-dimensional MoS_2/reduced graphene oxide aerogel as a macroscopic visible-light photocatalyst," *Chin. J. Catal.* **38**(2), 313–320 (2017).
34. G. A. M. Ali et al., "One-step electrochemical synthesis of MoS_2/graphene composite for supercapacitor application," *J. Solid State Electrochem.* **24**, 25–34 (2020).
35. M. M. Abdi et al., "Optical band gap and conductivity measurements of polypyrrole-chitosan composite thin films," *Chin. J. Polym. Sci.* **30**, 93–100 (2012).
36. H. Wang et al., "Preparation of MoS_2 nanosheets with large lateral size and thickness controllability by a two-step process," *J. Mater. Chem. C* **2**(30), 5987–5991 (2014).

37. I. R. Agool et al., "Improving the photoresponse of porous silicon for solar cell applications by embedding of CdTe nanoparticles," *Surf. Rev. Lett.* **24**(Supp01), 1850012 (2017).
38. A. H. Ismail, A. N. Abd, and H. K. Kareem, "Fabrication a solar cell by synthesize a new nano particles of quinoline derivative and its metal complex with studing the optical, structural and morphological properties," *J. Chem. Pharm. Sci.* **10**(4), 140–146 (2017).

Nagham M. Obaid earned a BSc in physics from the University of Babylon's College of Education in 2006 and an MSc in laser physics from the University of Babylon's College of Science for Women in 2016. Now she is a PhD student in the research stage at the University of Babylon's College of Science for Women. Her scientific interests are in the fields of lasers and their wide applications, and she has conducted several research projects in this field.

Amer Al-Nafiey earned a BSc in physics from the University of Babylon in 1998, an MSc in physics from the same university in 2006, and a PhD in nanotechnology from the Lille 1 University of Science and Technology in 2016. Now he is an academic researcher and assistant professor at the University of Babylon's College of Science for Women. His scientific interests are in the fields focused on nanomaterials, nanomaterials synthesis, material characterization, thin film synthesis, nanostructured materials, nanocomposites, carbon nanomaterials, catalysis, and bio-nanoapplications, and he has more than 30 research papers published in international peer-reviewed journals.

Ghaleb Al-Dahash earned a BSc in physics from Al-Mustansiriya University in 1986, an MSc in nuclear material physics from Al-Mustansiriya University in 1992, and a PhD in solid state physics with a focus on superconductivity from the University of Baghdad in 1998. Now he is a professor of physics at the University of Babylon's College of Science for Women. His scientific interests are in the fields of laser material processing and superconductors, and he has more than 86 research papers published in international peer-reviewed journals.